

Journal of Materials Chemistry C

Accepted Manuscript



This is an *Accepted Manuscript*, which has been through the Royal Society of Chemistry peer review process and has been accepted for publication.

Accepted Manuscripts are published online shortly after acceptance, before technical editing, formatting and proof reading. Using this free service, authors can make their results available to the community, in citable form, before we publish the edited article. We will replace this *Accepted Manuscript* with the edited and formatted *Advance Article* as soon as it is available.

You can find more information about *Accepted Manuscripts* in the [Information for Authors](#).

Please note that technical editing may introduce minor changes to the text and/or graphics, which may alter content. The journal's standard [Terms & Conditions](#) and the [Ethical guidelines](#) still apply. In no event shall the Royal Society of Chemistry be held responsible for any errors or omissions in this *Accepted Manuscript* or any consequences arising from the use of any information it contains.

Donor and Acceptor Impurities-Driven Switching of Magnetic Ordering in $\text{MnSb}_{2-x}\text{Sn}_x\text{Se}_4$

Honore Djeutedjeu¹, Xiaoyuan Zhou², Hang Chi², Neel Haldolaarachchige³, Kulugamma G. S. Ranmohotti¹, Ctirad Uher², David Young³, Pierre F. P. Poudeu^{1,}*

1) Laboratory for Emerging Energy and Electronic Materials (LE³M), Department of Materials Science and Engineering, University of Michigan, Ann Arbor, 48109, USA

2) Department of Physics, University of Michigan, Ann Arbor, MI, 48109, USA

3) Department of Physics and Astronomy, Louisiana State University, Baton Rouge, LA, 70803-4001, USA

Keywords: Bound Magnetic Polarons; Ferromagnetism Semiconductor; Spintronic; Manganese Selenides; Solid-Solution

*Corresponding author. Email: ppoudeup@umich.edu (PFPP); Fax: +1-734-763-4788

RECEIVED DATE.....

Abstract

The ability to manipulate the electronic structure of the low-dimensional magnetic semiconductor MnSb_2Se_4 via isomorphic Sn/Sb substitutions enables independent investigation of the interactions of free carriers with localized magnetic moments and their effects on the predominant magnetic ordering in the *p*-type $\text{MnSb}_{2-x}\text{Sn}_x\text{Se}_4$ ($0 \leq x \leq 0.25$) semiconductors. We find a large increase in the electrical resistivity and thermopower with increasing Sn content suggesting a surprising decrease in the overall holes density. X-ray photoelectron spectroscopy reveals that Sn atoms enter the structure in 2+ oxidation state, whereas a fraction of the remaining Sb^{3+} partially oxidizes to Sb^{5+} to maintain the electroneutrality of the compound. Therefore, we attribute the drop in the hole density to electron – hole compensation processes. Interestingly, magnetic susceptibility data reveal a remarkable switching of the dominant magnetic interaction from antiferromagnetism (AFM) ($x = 0$) to ferromagnetism (FM) with $T_c \sim 56$ K for $0.05 \leq x \leq 0.15$ samples and a reversal to AFM ordering $x > 0.15$. The Sn-dependent FM interaction in $\text{MnSb}_{2-x}\text{Sn}_x\text{Se}_4$ is rationalized within the context of the formation of overlapping bound magnetic polarons (BMPs) through the interactions between the added electrons/holes and localized moments of Mn^{2+} magnetic ions.

1. Introduction

There are currently widespread research activities in the fields of solid-state chemistry and solid-state physics focusing on the integration of semiconducting and magnetic functionalities within the same material and the manipulation of one property by the other.¹⁻³ Research efforts into the correlation between magnetism and transport properties over the past decades have focused on III-V and II-VI diluted magnetic semiconductors (DMSs) and diluted magnetic oxides (DMOs).⁴⁻⁸ The motivation for the choice of these material systems is dictated by the current structure of most electronics devices and the fact that doping these host materials with a transition metal (TM) element will not affect the processing and integration procedures. In addition, it was shown that such manipulation of the chemical composition of III-V, II-VI and oxide semiconductors leads to new materials with interesting magneto-optic, optoelectronic, nonlinear optic and photoelectric properties.⁹⁻¹¹ Long range FM ordering in DMSs and DMOs compounds is believed to originate from exchange interactions between localized moments and spin polarized carriers (holes or electrons).¹²⁻¹⁴ However, the fabrication of practical devices such as information storage and processing units, light emitting diodes and detectors based on these materials is severely hampered by their low Curie temperature (T_c).⁷⁻⁸ Understanding the mechanism of magnetic coupling in semiconductors is critically important to improving T_c values of DMSs and DMOs above 300K. Besides III-V, II-VI and V-VI DMSs and DMOs,¹⁵⁻¹⁶ magnetic semiconducting chalcogenides (MSCs) such as EuS, EuSe and CdCr₂Se₄,¹⁷⁻¹⁹ as well as V-VI tetradymite-type semiconductors doped with V and Cr,^{15, 20} have also been investigated. DMSs, DMOs and MSCs are complex magnetic systems in the sense that several types of interactions such as the double exchange interaction, the s-d and p-d exchange interactions, and the superexchange interaction are involved in the magnetic ordering. For instance, one must take into account contributions of electronic charge carriers (holes and electrons) in order to fully understand magnetic exchange interactions in such materials systems. Over the past two decades, significant advances have been made towards the fundamental understanding of the magnetism in III-V and II-VI semiconductors doped with Mn atoms.²¹⁻²³ In these systems, the Mn atoms act both as an acceptor (providing holes) and as the magnetically active species (providing localized magnetic moments) in the semiconducting hosts. While it is widely accepted that holes in Mn-doped DMSs mediate the interactions between adjacent magnetic centers (Mn – Mn) in the host material to induce ferromagnetism, it is vigorously debated whether holes introduced when Mn substitutes for Ga in (Ga,Mn)As reside within the valence band of the host or form an impurity band within the band gap of the host material.²⁴ From the

valence band concept, it was predicted that T_c increases monotonically with the increase of Mn concentration and the hole density.^{14, 25-30} The alternative model, which assumes that the holes reside in a Mn-derived impurity band, even for moderate or high Mn concentrations, also shows that T_c is related to the concentration of Mn and the hole density.^{4, 31-35} However, a more recent experimental study focusing on a simultaneous determination of the fraction of Mn atoms contributing to ferromagnetism and the hole density in (Ga,Mn)As suggested that the location of the Fermi level within the impurity band (i.e. the degree of hole localization), rather than the hole concentration determines T_c .²⁴ These contradictory reports underscore the difficulty to fully understand the correlations among electronic transport, magnetic ordering, and chemical composition in traditional Mn-doped DMSs. This is due to the fact that both the concentration of impurity states (holes) responsible for the electrical conduction, and the concentration of localized spins from the half-filled 3d Mn^{2+} shells responsible for the ferromagnetism in DMSs, are altered simultaneously when, for example, Mn ions substitute for Ga in (Mn,Ga)As. The complexity of the magnetism in DMSs, DMOs and MSCs is further increased by the fact that under external applied fields, spin-polarized electronic charge carriers can cluster into magnetic polarons.^{36-37,38-39}

In magnetic semiconductors, bound magnetic polarons (BMPs) can be anticipated in the presence of non-ionized acceptors or donors.⁴⁰ The polarons result from the interaction of the localized carriers (holes, electrons) with phonon and are coupled antiferromagnetically with number of magnetic impurities within its localized radius. Therefore, localized spins on magnetic impurities within the orbit of the same polaron are aligned ferromagnetically. However, the BMPs effect is only observed when the concentration of donor or acceptors is relatively high, but not too high to create impurity bands.³ The size of BMP increases with the ratio of the exchange interactions and the thermal energy, causing the BMPs to overlap at sufficiently low temperatures to give long range FM exchange interaction between the percolated polarons. In such magnetic systems a discrepancy between the effective magnetic moment from Curie-Weiss law and the theoretical value is generally observed. For example, Co-doped TiO_2 exhibits giant magnetic moments of $7.2 \mu_B/Co$ in Co^{2+} , while the value expected theoretically from the spin-only formula is $3 \mu_B$ in a high spin state.²³ Therefore, to fully understand magnetic coupling in semiconductors, one must find a way to independently control (1) the nature, concentrations and distribution of the magnetic ions (localized magnetic moments), and (2) the fraction of magnetic polarons in the material.

Low symmetry ternary and quaternary transition-metal chalcogenides have emerged as rich playgrounds for independent systematic investigations of electronic transport and magnetic exchange interactions in magnetic semiconductors and could enable a fundamental understanding of correlations between both properties within a single crystal structure.^{9-11, 41-45} For instance, we have recently identified the homologous series of magnetic semiconductors with the general formula, $M_2Pn_4Sn_{N-3}Se_{N+5}$ ($Pn = Sb, Bi; M = Mn, Fe; N \geq 3$).^{9, 41-42, 45} Members of this series of compounds adopt closely related structures formed by two distinct building units. In the crystal structure (**Figure 1A**), two types of building units, denoted A and B alternate along [001]. The unit A is identical for all members of the homologous series and is built of paired rods of face-sharing monocapped trigonal prisms around Pn atoms alternating along the *a*-axis with a single chain of edge-sharing octahedra around the magnetic M atoms. Various members of the series can be discriminated by the thickness of the NaCl-type building unit B separating adjacent units A, where the thickness of unit B is defined by the number N of edge-sharing octahedra running across its diagonal. Therefore, the composition and structure of various members of the $M_2Pn_4Sn_{N-3}Se_{N+5}$ ($N \geq 3$) series can be derived for each value of N. The first member of the series with $N = 3$ corresponds to the fascinating class of ternary compounds MPn_2Q_4 ($M = Fe, Mn; Pn = Sb, Bi; Q = S, Se$). Our investigation of the crystal structure, magnetic properties and electronic transport properties of several compositions of the MPn_2Q_4 phases ($MnSb_2Se_4$,⁴¹ $FeSb_2Se_4$,⁴² and $Mn_{1-x}Sn_xBi_2Se_4$ ⁴⁵) revealed that, despite the structural similarity of these phases, their magnetic behavior is defined by the nature of magnetic atoms within the $[M_nSe_{4n+2}]$ chains (**Figure 1B**) of edge-sharing octahedra (*magnetic subunit*). For instance, the dominant type of magnetic ordering in MPn_2Se_4 can be tuned from FM⁴² to AFM^{41, 45} by altering the nature of the transition metal atoms within the $[M_nSe_{4n+2}]$ chain from Fe to Mn. Likewise, the dominant charge carrier type in MPn_2Se_4 can be manipulated by altering the composition of the $[Pn_2Se]$ network (*semiconducting subunit*) separating adjacent $[MSe_6]$ chains in the structure. For example, substituting Sb for Bi at the Pn sites in MPn_2Se_4 induces drastic change in the conduction type from *p*-type for MSb_2Se_4 ^{41 42} to *n*-type for MBi_2Se_4 .⁴⁵ Recently, we showed that the dominant AFM ordering in $MnBi_2Se_4$ can be switched into weak FM interactions with $T_c \sim 55$ K upon partial substitution of Mn by Sn within the magnetic subunit ($[M_nSe_{4n+2}]$ magnetic chains) accordingly with the formula $Mn_{1-x}Sn_xBi_2Se_4$.⁴⁵ Here, we demonstrate that by altering the hole density through Sb – to – Sn substitution within the semiconducting unit, and without changing the concentration of Mn atoms within the magnetic subunit, the nature of the dominant magnetic interaction in $MnSb_{2-x}Sn_xSe_4$ can be switched from the AFM

ordering observed in the parent compound ($x = 0$) to FM ordering with $T_c \sim 56$ K for Sn-doped samples with $0.01 \leq x \leq 0.15$, followed by a reversal to AFM ordering for samples with higher Sn content. This surprising alteration in the magnetic behavior of $\text{MnSb}_{2-x}\text{Sn}_x\text{Se}_4$ compositions is rationalized within the context of the formation of various fractions of overlapping bound magnetic polarons (BMPs) in various $\text{MnSb}_{2-x}\text{Sn}_x\text{Se}_4$ samples. X-ray photoelectron spectroscopy (XPS) indicated that partial substitution of Sb^{3+} by Sn^{2+} led to the oxidation of a small fraction of Sb^{3+} to Sb^{5+} dumping additional electrons in the p -type $\text{MnSb}_{2-x}\text{Sn}_x\text{Se}_4$ matrix. The interactions between the added electrons and localized magnetic moments within individual magnetic chains result in the formation of BMPs, which is believed to be responsible for the dominant FM magnetic ordering in various samples.

2. Experimental Section

Synthesis: Single-phase polycrystalline powders of $\text{MnSb}_{2-x}\text{Sn}_x\text{Se}_4$ ($0 \leq x \leq 0.25$) were obtained through solid-state reaction of the elements at moderate temperatures. Stoichiometric mixtures of high purity elements (99.999%, from Cerac), were roughly mixed under argon atmosphere in a dry glove box using an agate mortar with pestle and sealed in an evacuated quartz tube with a residual pressure of $\sim 10^{-3}$ Torr. The sealed tubes were then placed in a furnace and the temperature was ramped to 573 K at 48 K/h and dwelled for 24 h. This first step is required to allow elements with low melting temperatures (Se, Sn) to react completely with the other elements and to avoid any explosive reactions. The temperature was then ramped up to 773K over 12 h and dwelled there for 72 h, and finally cooled slowly to room temperature over 48 hours. The resulting products were dark gray polycrystalline powders.

Powder X-ray Diffraction (PXRD): X-ray powder diffraction (XRD) data were recorded on a rotating anode Rigaku powder diffractometer operating under 40 kV and 40 mA using a monochromated Cu $K\alpha$ radiation ($\lambda = 1.5418$ Å). Standard X-ray data were collected in a step-scanning mode with a 0.02° step width and 10 s count time in the 2θ range of 10° - 70° . The cell parameters were refined by the Rietveld method using the FullProf software package.⁴⁶⁻⁴⁷ Refinement results are given in Table 1 and atomic positions of selected compositions are gathered in Table 2.

X-ray Photoelectron Spectroscopy (XPS): To probe the chemical composition as well as determining the oxidation states of Mn, Sn, and Sb in the synthesized $\text{MnSb}_{2-x}\text{Sn}_x\text{Se}_4$ materials, XPS spectra of selected samples were recorded under the same condition on a Kratos Axis Ultra XPS using a monochromated aluminum anode.

Charge Transport Measurements: Electrical resistivity (ρ) and thermopower (S) were measured simultaneously from 140 K to 300 K using (1) the standard four-probe method in a Quantum Design Physical Property Measurement System (PPMS) and (2) the four-probe longitudinal steady-state technique using a liquid ^4He cryostat. In the latter method, samples were mounted on the cryostat and protected from excessive radiation loss by two radiation shields. One end of the sample was attached to a heat sink by indium solder. The heat sink was the cold tip of the liquid helium cryostat, and the temperature was adjusted using a Lakeshore 340 temperature controller. Heat input to the sample was made via a small 350- Ω strain gauge heater attached to the free end of the sample using varnish. The heat flow injected by the heater developed a temperature difference ΔT between the two points along the length of the sample. Fine copper (Cu) wires were selected as Seebeck / resistive probes due to their small resistivity and thermopower.

Magnetic Measurements: Direct current (DC) and alternating current (AC) magnetic susceptibility measurements were performed on approximately 40 mg to 70 mg of polycrystalline $\text{MnSb}_{2-x}\text{Sn}_x\text{Se}_4$ powder using a Superconducting Quantum Interference Device (SQUID). DC susceptibility data in field cooled (FC) and zero field cooled (ZFC) modes were recorded over a temperature range from 2 K to 300 K with an applied magnetic field of 100 Oe. The AC susceptibility at different frequencies was collected on the same sample used for the DC measurements. The applied magnetic field used for the AC magnetic susceptibility was 0.1 Oe and data were collected within the temperature range between 5 K and 100 K. Field-dependent magnetization measurements were performed at 4 K on the samples with $x = 0.05, 0.1$ and 0.15 under applied magnetic fields up to 5 kOe.

3. Results and Discussions

3.1. Synthesis and Structure

Polycrystalline powders of $\text{MnSb}_{2-x}\text{Sn}_x\text{Se}_4$ ($0 \leq x \leq 0.25$) were easily obtained from solid-state reaction of the elements in the desired ratios. The single phase nature of the synthesized materials was confirmed by comparison of the experimental X-ray powder diffraction pattern of various compositions with the theoretical pattern calculated from the single crystal structure refinement data of the parent compound (MnSb_2Se_4). The excellent match between the experimental and theoretical patterns (**Figure 2A**) suggests that the synthesized $\text{MnSb}_{2-x}\text{Sn}_x\text{Se}_4$ phases are isostructural up to $x = 0.25$, which corresponds to the substitution of 12.5% Sb in the structure of MnSb_2Se_4 with Sn atoms. This isomorphic substitution of Sb by Sn in $\text{MnSb}_{2-x}\text{Sn}_x\text{Se}_4$ is quite surprising given the large difference ($\Delta R/R \sim 22\%$) in the ionic

radii of Sb^{3+} (76 pm) and Sn^{2+} (93 pm) in a six-fold coordination (CN = 6).⁴⁸⁻⁴⁹ Therefore, an expansion of the unit cell volume of $\text{MnSb}_{2-x}\text{Sn}_x\text{Se}_4$ with increasing Sn content (x value) can be expected. However, a careful refinement of the unit cell parameters (Table 1) using the Rietveld method revealed a strong anisotropic change in the lattice constants and a decrease of the unit cell volume with increasing Sn content. A plot of relative variations in the unit cell parameters of various $\text{MnSb}_{2-x}\text{Sn}_x\text{Se}_4$ ($0 \leq x \leq 0.25$) compositions (**Figure 2B**) shows that the c -axis initially expands by $\sim 0.7\%$ for compositions with $0.01 \leq x \leq 0.15$ and contracts drastically with further increase in Sn content. A similar trend is observed for the change in the beta angle. However, the a -axis marginally expands with increasing Sn content, while the b -axis remains nearly constant with increasing Sn content up to $x = 0.15$ and sharply increases with further increase in Sn concentration. This anisotropic change in the unit cell parameters resulted in a small decrease of the unit cell volume for composition with up to $x = 0.15$ substitution of Sb by Sn, followed by a drastic ($\Delta V/V > 2\%$) contraction for higher Sn content. The observed strong perturbation of the c -axis suggests that the substitution sites for Sn in the crystal structure of $\text{MnSb}_{2-x}\text{Sn}_x\text{Se}_4$ are predominantly the Sb positions (Figure 1). Our previous investigation of the crystal structure of the $\text{Mn}_{1-x}\text{Sn}_x\text{Bi}_2\text{Se}_4$ solutions, which also crystallize with the MnSb_2Se_4 structure type, revealed a strong preference for Mn over Sn at the $2a$ (0, 0, 0) and $2d$ (0, $\frac{1}{2}$, $\frac{1}{2}$) sites.⁴⁵ Therefore, it is reasonable to anticipate a strong preferential occupation of the $2a$ and $2d$ sites by Mn atoms in the structure of $\text{MnSb}_{2-x}\text{Sn}_x\text{Se}_4$ solid solutions (Figure 1). Within this atomic distribution picture, one can attribute the initial expansion of the c -axis to the substitution of the small Sb^{3+} ions by slightly larger Sn^{2+} ions in the structure of $\text{MnSb}_{2-x}\text{Sn}_x\text{Se}_4$. However, this simple one-on-one substitution between Sb^{3+} and Sn^{2+} ions cannot explain the sharp contraction of the c -axis observed for compositions with $x > 0.15$. In addition, a substitution between Sb^{3+} and Sn^{2+} should result in a gradual increase of the c -axis rather than the observed constant $\sim 0.7\%$ expansion for compositions with x ranging from 0.01 to 0.15.

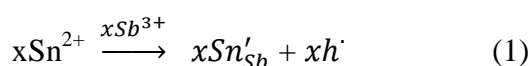
To better understand the observed changes in the unit cell parameters of the $\text{MnSb}_{2-x}\text{Sn}_x\text{Se}_4$ compounds, we have examined the oxidation states of various metal atoms (Mn, Sn, Sb) in various samples using X-ray photoelectron spectroscopy (XPS). Careful analysis of the XPS spectra (Figure 3) of samples with $x = 0, 0.1, 0.15, 0.2$ and 0.25 , revealed the presence of all expected elements. The observed gradual increase in the intensity of the $\text{Sn}_{3d_{5/2}}$ peak in various samples is consistent with the increase of Sn content in the $\text{MnSb}_{2-x}\text{Sn}_x\text{Se}_4$ nominal starting compositions (**Figure 3A**). Interestingly, the position of the $3d_{5/2}$ peak remains constant at 486.2 eV in all recorded samples. This value of the $\text{Sn}_{3d_{5/2}}$ binding energy is

similar to that of the $3d_{5/2}$ peak (486.1 eV) reported in SnSe and $Mn_{1-x}Sn_xBi_2Se_4$.^{45, 50} Therefore, one can conclude that the chemical state of Sn atoms in all $MnSb_{2-x}Sn_xSe_4$ samples is $2+$. No additional peaks at higher energies that can be assigned to Sn^{4+} were observed on the recorded XPS spectra. **Figure 3B** shows the XPS spectra of $Mn_{2p_{3/2}}$ in various $MnSb_{2-x}Sn_xSe_4$ samples. The binding energy of $Mn_{2p_{3/2}}$ peaks in all samples is ~ 641 eV, which is comparable with the binding energy (~ 640.2 eV) reported for the $Mn^{2+}_{2p_{3/2}}$ peak in MnSe.⁵¹ This indicates that Mn atoms in the synthesized $MnSb_{2-x}Sn_xSe_4$ samples remain in the $2+$ valence state regardless of the Sn content. The XPS spectra of the $Sb_{3d_{5/2}}$ peak recorded on $MnSb_{2-x}Sn_xSe_4$ samples are shown in **Figures 3C**. The binding energy of the $Sb_{3d_{5/2}}$ peak in the sample with $x = 0$ ($MnSb_2Se_4$) is 530.2 eV, which is consistent with the value of 529.3 eV reported for the $Sb_{3d_{5/2}}$ peak in Sb_2S_3 .⁵² Upon increasing the Sn content (increasing x value), there is a gradual shift of the $Sb_{3d_{5/2}}$ peak to higher binding energy (531 eV for $x = 0.1$ and 531.5 eV for $x = 0.15$) leading to the appearance of a shoulder peak at 531.8 eV (for $x = 0.2$) and 532.2 eV (for $x = 0.25$). Interestingly, the intensity of the shoulder peak increases with increasing Sn content from $x = 0.2$ to $x = 0.25$. The presence of the high energy shoulder $Sb_{3d_{5/2}}$ peak suggests the oxidation of a fraction of Sb^{3+} to Sb^{5+} with increasing Sn content. The observed binding energies of the $Sb_{3d_{5/2}}$ peaks from Sb^{3+} (530.2 eV) and Sb^{5+} (~ 531.5 eV) in $MnSb_{2-x}Sn_xSe_4$ samples are consistent with the results found for $Sb_{3d_{5/2}}$ peaks in Sb_2O_3 (529.7 eV) and Sb_2O_5 (531.3 eV)⁵³. Therefore, we can conclude that partial substitution of Sb^{3+} (76 pm) by Sn^{2+} (93 pm) in $MnSb_{2-x}Sn_xSe_4$ samples results in the oxidation of a small fraction of the remaining Sb^{3+} into Sb^{5+} (60 pm), while the valence state of Mn^{2+} remains constant.

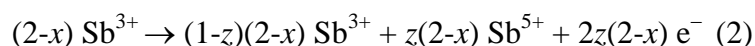
Based on XPS results, one can argue that the observed constant relative change in the c -axis with Sn content ranging from $x = 0.01$ to $x = 0.15$ (Figure 2B) is due to the oxidation of a small fraction of Sb^{3+} (76 pm) ions into smaller Sb^{5+} (60 pm) ions, which compensates for the increase in the c -axis expected from the substitution of Sb^{3+} (76 pm) by larger Sn^{2+} (93 pm) ions. For $MnSb_{2-x}Sn_xSe_4$ samples with Sn content above $x = 0.15$, a significantly larger portion of Sb^{3+} is oxidized to Sb^{5+} leading to the observed sharp decrease in the c -axis. In addition, the sharp contraction of the c -axis for $x > 0.15$ can be further rationalized by taking into account the stereoactivity of the Sb electron “lone pair”. In the crystal structure of $MnSb_2Se_4$ (Figure 1A), the orientation of the Sb electron “lone pair” (along the c -axis) results in a large separation between adjacent layers (broken bonds). The substitution of a large fraction of Sb^{3+} by Sn^{2+} in $MnSb_{2-x}Sn_xSe_4$ samples induces the oxidation of a large fraction (see equation (3)) of the remaining lone-pair bearing Sb^{3+} ions into Sb^{5+} , which is “lone-pair”

free. For composition with $x = 0.15$, 15% of the remaining Sb atoms are at the 5+ oxidation state, according to the chemical reaction (3). The fraction of Sb^{5+} increases to 22% and 29% for samples with $x = 0.2$ and 0.25 , respectively. This large fraction of lone-pair free Sb^{5+} ions at the Sb sites minimizes the effect of the stereoactivity of the Sb electron “lone pair” against lattice contraction leading to a sharp reduction in the unit cell volume.

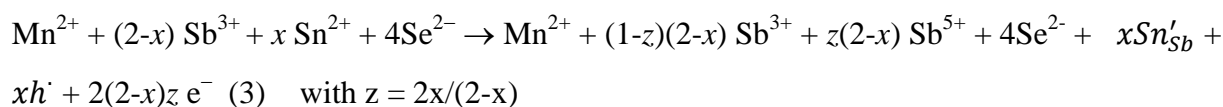
To understand the driving force triggering the oxidation of Sb^{3+} into Sb^{5+} , one must carefully consider the alteration of the charge balance in $\text{MnSb}_{2-x}\text{Sn}_x\text{Se}_4$ samples upon substituting Sb^{3+} by Sn^{2+} . A one-to-one substitution of Sb^{3+} by Sn^{2+} at Sb sites in the structure of MnSb_2Se_4 creates local excess of negative charges on the cation sublattice and acceptor states (extrinsic holes) within the band gap, accordingly with equation (1).



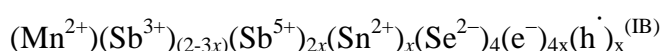
The local excess negative charges are balanced by the oxidation of a fraction of the remaining Sb^{3+} ions into Sb^{5+} followed by the generation of additional free electrons, according to reaction (2).



The charge balanced chemical equation for the substitution and oxidation processes is given by



Therefore, the chemical formula of the substituted compounds is



It follows from this chemical formula that the substitution of x moles of Sb^{3+} in MnSb_2Se_4 by an equivalent number of moles of Sn^{2+} induces the formation of $2x$ moles of Sb^{5+} , which generates $4x$ moles electrons and x moles of holes (acceptor states) in the MnSb_2Se_4 matrix. This alteration of the electronic structure of $\text{MnSb}_{2-x}\text{Sn}_x\text{Se}_4$ compounds with increasing Sn content is expected to induce drastic changes in the electronic and magnetic properties of the resulting compound.

3.2. Electronic Transport Properties

To probe the effect of Sn for Sb substitutions on the electronic transport properties of $\text{MnSb}_{2-x}\text{Sn}_x\text{Se}_4$ samples, we have measured the electrical conductivity and thermopower in the temperature range from 300 K to 140 K (**Figure 4**). At a given temperature, the electrical resistivity of $\text{MnSb}_{2-x}\text{Sn}_x\text{Se}_4$ samples rapidly increases with increasing Sn content. For

example, at 200 K the electrical resistivity of the sample with $x = 0$ (matrix) is $\sim 10^3 \Omega\cdot\text{m}$ and rapidly increases upon Sn substitution to $6 \times 10^3 \Omega\cdot\text{m}$ for the composition with $x = 0.01$ (**Figure 4A**). The electrical resistivity at 200K increases by an order of magnitude ($1.4 \times 10^4 \Omega\cdot\text{m}$) after substitution of $x = 0.1 \text{ Sn}^{2+}$ for Sb^{3+} (**Figure 4B**) and increases by three orders of magnitude ($2.3 \times 10^6 \Omega\cdot\text{m}$) upon increasing Sn content to $x = 0.25$ (**Figure 4C**). Regardless of the composition, the electrical resistivity drastically decreases with increasing temperature suggesting semiconducting behavior. However, the onset temperature of the observed sharp increase in the resistivity of various samples on cooling increases from 200 K for $x = 0$ to 250 K for $x = 0.25$ (Figure 4A). For each composition, the electrical resistivity increases (within a narrow temperature window) by several orders of magnitude upon further cooling below the onset temperature. At 300 K, the electrical resistivity increases from $9 \Omega\cdot\text{m}$ for the parent compound ($x = 0$) to $14 \Omega\cdot\text{m}$ and $35 \Omega\cdot\text{m}$ for $x = 0.01$ and $x = 0.1$, respectively. Further increasing the Sn content to $x = 0.25$ resulted in a sharper rise of the electrical resistivity to $8.5 \times 10^4 \Omega\cdot\text{m}$ at 300 K (Figure 4C). The observed sharp increase in the electrical resistivity with increasing Sn substitution suggests that a large fraction of extra electrons generated through the oxidation of Sb^{3+} to Sb^{5+} (chemical equation (2)) compensate intrinsic holes (existing holes) within the valence band of $\text{MnSb}_{2-x}\text{Sn}_x\text{Se}_4$ compounds, leading to a large drop in the density of free-holes in the VB. The magnitude of the drop in the hole density at a given temperature increases with Sn content (x values). For instance, the substitution of $x = 0.01 \text{ Sb}^{3+}$ by Sn^{2+} is expected to increase the electron density of the compound by $\sim 2.24 \times 10^{20}$ electrons/ cm^3 , and create $\sim 5.59 \times 10^{19}$ acceptor states/ cm^3 within the band gap (chemical equation (3)). The density of existing holes in the MnSb_2Se_4 parent compound is very small ($< 1 \times 10^{18}/\text{cm}^3$), given its very large electrical resistivity and Seebeck coefficient.⁴¹ Therefore, a fraction of the added electrons combines with the intrinsic holes (**Figure 5B**) leading to large decrease in the effective hole density at 0 K. This explains the large increase in the electrical resistivity of the sample with $x = 0.01$ compared to the un-substituted matrix (Figure 4A). The remaining added electrons are either localized within the Sn^{2+} acceptor states or form donor impurity states within the band gap. As the temperature increases, the electrical resistivity rapidly decreases following a thermally activated behavior (**Figure 5C**). This indicates that thermally excited electrons populate a fraction of acceptor states within the band gap. The activation energy extracted from the fitting of the electrical resistivity curve using the Arrhenius law is 0.31 eV, which is 0.05 eV higher than the activation energy calculated for the un-substituted sample (0.26 eV). This suggests a decrease in the energy of the

compensated electron-hole pairs ($\sim 2.24 \times 10^{20}$ pairs/cm³). Increasing the concentration of Sn²⁺ to $x = 0.1$ results in the creation of $\sim 2.24 \times 10^{21}$ electrons/cm³, and $\sim 5.59 \times 10^{20}$ acceptor states/cm³ in the MnSb_{2-x}Sn_xSe₄ matrix. The increase in the concentration of added electrons compared to the sample with $x = 0.01$, implies that at 0 K, a larger fraction of acceptor states will be occupied by extra electrons after electron compensation of intrinsic holes. Therefore, only a small fraction of thermally excited electrons can be accommodated within the acceptor states upon heating. This explains the observed larger increase in the electrical resistivity in the whole temperature range as well as the increase of the onset temperature of the sharp rise in the electrical resistivity upon cooling when compared to the sample with $x = 0.01$ (Figures 4A and 4B). The calculated activation energy for thermal excitation of carriers into the Sn²⁺ acceptor states is ~ 0.32 eV. For the sample with $x = 0.25$, the generation of even a larger density of electrons ($\sim 5.6 \times 10^{21}$ electrons/cm³) and acceptor states ($\sim 1.4 \times 10^{21}$ acceptor states/cm³) is anticipated. This is consistent with the observed higher electrical resistivity at all temperatures (Figure 4C) of the sample with $x = 0.25$ compared to the sample with lower Sn content. The activation energy for thermal excitation of carriers into the Sn acceptor states is estimated to be ~ 0.25 eV, which is comparable to that of the un-substituted matrix. This decrease in the activation energy for the sample with $x = 0.25$ compared to samples with $x = 0.01$ and 0.1 is attributed to the sharp contraction observed in the unit cell volume for samples with high Sn content. These values of the activation energy along with the measured optical band gap of 0.32 eV for $x = 0$ indicate that MnSb_{2-x}Sn_xSe₄ compositions are narrow band gap semiconductors.

Figure 4D shows the temperature dependent thermopower plots of selected MnSb_{2-x}Sn_xSe₄ samples ($x = 0, 0.01, \text{ and } 0.1$). All samples show positive thermopower values indicating *p*-type semiconducting behavior in the measured temperature range. Regardless of the composition, the thermopower rapidly increases with decreasing temperature, suggesting freezing of a large fraction of holes upon cooling. This is consistent with the thermally activated behavior of the electrical resistivity as discussed above. At a given temperature, the thermopower rapidly increases with increasing Sn content. This suggests that a large fraction of electrons dumped into the VB through the oxidation of Sb³⁺ to Sb⁵⁺ remain trapped there as electron-hole pairs, leading to a reduction in the hole density. For example, the thermopower of the sample with $x = 0.1$ is +1122 $\mu\text{V/K}$ at 300K, which corresponds to a 19% increase when compared to the thermopower of the MnSb₂Se₄ sample (+942 $\mu\text{V/K}$ at 300 K). It follows from the above discussion of the electrical resistivity and thermopower data that the substitution of Sb³⁺ by Sn²⁺ in the *p*-type MnSb₂Se₄ compound results in the generation of a

large density of electrons ($\sim 10^{21}$ /cm³) and a large concentration of Sn acceptor states ($\sim 10^{21}$ /cm³). The added electrons form compensated electron-hole pairs in the VB leading to a large increase in the electrical resistivity and thermopower.

3.3. Magnetic Properties

The observed alteration of the electronic structure arising from the substitution of Sb³⁺ by Sn²⁺ in the structure of MnSb₂Se₄ is expected to drastically influence the magnetic behavior of the resulting compound. For instance, it was observed that a large density of free electrons is generated through the Sb³⁺ to Sb⁵⁺ oxidation process and a high concentration of acceptor states are also created within the band gap of the MnSb₂Se₄. Therefore, it can be anticipated that at temperatures above 0 K, thermal activation processes can lead to the population of a fraction of the acceptor states by electrons. Since these acceptor states are immobile, one can anticipate the formation of localized spin-polarized electrons throughout the sample upon application of an external magnetic field. In the crystal structure of the MnSb₂Se₄ phase, the magnetic atoms (Mn) are essentially located within the magnetically quasi-isolated Mn_nSe_{4n+2} single chains of edge-sharing octahedra, which are 6.998(2) Å and 7.668(2) Å apart (**Figure 1A**). Therefore, the magnetic behavior of the MnSb₂Se₄ phase is essentially dominated by the intra-chain magnetic exchange interactions. However, the presence of spin-polarized localized electrons within the semiconducting network separating neighboring magnetic chains in the structure of MnSb_{2-x}Sn_xSe₄ composition is expected to influence magnetic exchange interactions between neighboring magnetic chains. To investigate the magnetic behavior of the MnSb_{2-x}Sn_xSe₄ compounds, we measured the temperature dependence of both the ZFC and FC molar susceptibilities of several samples with different Sn concentrations under 100 Oe applied field (**Figure 6A**). Temperature dependent magnetic susceptibility data for the Sn-free composition (MnSb₂Se₄)⁴¹ features a broad downturn at T_N = 20 K, suggesting AFM exchange interactions between localized spins on the nearest neighboring Mn atoms within individual Mn_nSe_{4n+2} single magnetic chains (**Figure 6A**). The linear fit of the inverse susceptibility between 120 K and 300 K using the Curie-Weiss law resulted in a negative Weiss constant $\theta = -74$ K, and the calculated effective magnetic moment of $\mu_{\text{eff}(\text{calc})} = 5.82 \mu_{\text{B}}$ /Mn atom (**Table 2**) is slightly smaller than the expected theoretical spin-only value of 5.92 μ_{B} for Mn²⁺ (3d⁵) in the high-spin configuration. Upon Sn doping at the Sb sites in the structure of the MnSb_{2-x}Sn_xSe₄ phases, a marginal alteration in the magnitude of the molar susceptibilities is observed between 300 K and 56 K for various Sn concentrations. However, the magnetic susceptibilities for all samples gradually increase with decreasing temperature

from 300 K to 56 K. Surprisingly, further cooling below 56 K revealed a drastic variation in the temperature dependent magnetic susceptibilities of Sn-substituted samples. For instance, a noticeable increase in the magnitude of the magnetic susceptibility is observed below 56 K for the composition with $x = 0.01$ when compared to that of the Sn-free sample. A drastic increase in the magnitude of the susceptibility is observed for Sn concentrations ranging from $x = 0.05$ to $x = 0.15$, with the largest susceptibility values observed for the sample with $x = 0.05$. The sudden increase in the susceptibility values between 56 K and 40 K for the compositions with $x = 0.01, 0.05, 0.1$ and 0.15 is associated with the onset of local FM in the samples. Below 40 K, the slope of the susceptibility curves drops, suggesting a competition between the local FM and the intrinsic AFM super-exchange interaction within the $\text{Mn}_n\text{Se}_{4n+2}$ single magnetic chains (Figures 6A). Interestingly, the FM observed in samples with low Sn concentrations ($0.01 \leq x \leq 0.15$) vanishes in samples with higher Sn content ($x > 0.15$), and a drastic drop in the susceptibility is observed below 56 K.

The temperature dependent inverse susceptibility data between 120 K and 300 K for all Sn-substituted samples follow the Curie-Weiss law. The Weiss and Curie constants, as well as the effective magnetic moments extracted from the linear fits of the inverse susceptibility data, are shown in Table 3. Smaller Weiss constant values (compared to the Sn-free sample) and effective magnetic moments larger than the theoretical value of $5.92 \mu_B$ expected from Mn^{2+} ions ($3d^5$) were observed for samples with $x = 0.01, 0.05, 0.1$ and 0.15 (Table 3). Furthermore, isothermal field dependence of the magnetization performed at 4 K in the 0-5 kOe range (Figure 6B) showed magnetic hysteresis with a coercive field, $H_c = 150$ Oe. However, saturation of the magnetization was not observed up to an applied field of 10 kOe. These results further confirmed that at the optimum Sn concentration the $\text{MnSb}_{2-x}\text{Sn}_x\text{Se}_4$ phases retain a small FM character at low temperatures despite the competing intrinsic intra-chain AFM interactions. Samples with Sn content above $x = 0.15$ showed larger negative Weiss constants and larger effective magnetic moments when compared to the pristine composition. This suggests that local FM in these samples ($x > 0.15$) are dominated by the strong AFM exchange interactions within individual $\text{Mn}_n\text{Se}_{4n+2}$ single magnetic chain.

To further probe the nature of the magnetic ordering in the $\text{MnSb}_{2-x}\text{Sn}_x\text{Se}_4$ phases ($x = 0.01, 0.05, 0.15$ and 0.25), we performed temperature dependent alternating current (AC) susceptibility at different frequencies under an applied field of 0.1 Oe. Figure 7 shows the temperature dependence of the in-phase part (χ') of the AC susceptibility of samples with different compositions under various frequencies. It was observed that the AC susceptibility (χ') for most samples (except the composition with $x = 0.01$) is frequency independent. For

the composition with $x = 0.01$, χ' gradually increases with decreasing temperature and exhibits two distinct peaks at 76 K and 21 K (**Figure 7A**). The sharp peak observed around 76 K for this particular sample appears only when frequencies between 750 Hz and 1000 Hz are used and suggests the presence of a frustrated FM presumably from spin-polarized localized electrons. The peak around 21 K, however, can be associated with magnetic frustration arising from the competition between AFM within individual $\text{Mn}_n\text{Se}_{4n+2}$ single magnetic chains and weak FM of spin-polarized localized electrons in the compound. For the compositions with $x = 0.05$ and $x = 0.15$, the shape of the temperature dependent in-phase susceptibility curves (**Figure 7B and 7C**) are very similar to the corresponding ZFC DC susceptibility curves (**Figure 5A**). The sharp increase in the in-phase AC susceptibility observed at 56 K indicates onset of FM in the samples ($x = 0.05$ and $x = 0.15$). However, the in-phase AC susceptibility curves feature a broad downturn between 45 K and 15 K, which is followed by a steeper drop in the susceptibility upon further cooling. The broad downturn in the AC susceptibility curves suggests a competition between the FM observed at 56 K and the intrinsic AFM within the $\text{Mn}_n\text{Se}_{4n+2}$ single magnetic chains. Below 15 K, this competition is dominated by the intra-chain AFM interactions leading to a sharp drop in the magnetic susceptibility. For the composition with $x = 0.15$, a frequency-independent and nearly linear increase in the in-phase AC susceptibility with decreasing temperature was observed (**Figure 7D**), suggesting the absence of any magnetic ordering at this composition. However, the large negative values of the Weiss constant (**Table 3**) suggest the presence of strong AFM interactions in $\text{MnSb}_{2-x}\text{Sn}_x\text{Se}_4$ compositions with Sn content greater than $x = 0.15$.

The above magnetic data clearly indicate that the dominant magnetic interaction in various $\text{MnSb}_{2-x}\text{Sn}_x\text{Se}_4$ phases strongly depends on the fraction of Sn atoms in the compound. Starting from the AFM MnSb_2Se_4 phase, it was found that FM interaction with $T_c = 56$ K can be induced through partial isomorphic substitution of Sn at Sb sites in the structure of $\text{MnSb}_{2-x}\text{Sn}_x\text{Se}_4$ ($0.01 \leq x \leq 0.15$). Interestingly, this FM vanishes upon further increase of the Sn content above $x = 0.15$. Although the complete mechanism leading to the drastic changes that govern the magnetic ordering in $\text{MnSb}_{2-x}\text{Sn}_x\text{Se}_4$ is not fully understood, a plausible explanation of the observed data must take into account changes in the electronic structure within this system upon isomorphic substitution of Sn at Sb sites, as well as the interaction of the magnetic cations (Mn) with added electrons within the acceptor states. As discussed above, the substitution of Sb^{3+} by Sn^{2+} induces a large concentration of electrons and acceptor states within the band gap of the compounds leading to the formation at low temperatures of localized spin-polarized carriers within the Sn^{2+} impurity band. The density of such spin-

polarized electrons at temperatures below which thermal activation is negligible ($T < 100$ K) depends on the concentration of Sn (x) which controlled both the density of electrons added and the concentration of Sn^{2+} acceptor states formed. The remaining fraction of added electrons after electron-hole compensation either occupied a portion of available acceptor states within the band gap (Figure 5B) or formed new donor states. This results in the formation of localized (for low Sn content) or delocalized (for high Sn content) spin-polarized electrons (hydrogenic electrons) with the band gap. Localized spin-polarized hydrogenic electrons are obtained within the band gap when acceptor states occupied by electrons are not overlapping to form an impurity band. This condition is best realized for $\text{MnSb}_{2-x}\text{Sn}_x\text{Se}_4$ compositions with low Sn content ($x \leq 0.15$), in which the concentration of acceptor states with a single electron is small. Under the application of an external magnetic field, such localized electrons tend to form bound magnetic polarons (BMPs).^{40, 54} That is the clustering of a large number of spin-polarized localized electrons around magnetic ions (Figure 8). The BMPs interact with 3d moments of Mn^{2+} magnetic ions within their orbits.^{6, 38} For Mn^{2+} ions with a $3d^5$ half-full shell, the interaction with the localized hydrogenic electron is antiferromagnetic.⁶ Therefore, two Mn^{2+} ions falling within the orbit of the same localized electron will be coupled ferromagnetically. The size of such BMPs at a given temperature grows with increasing density of localized hydrogenic electrons (increasing x value), and the overlap of neighboring BMPs results in parallel alignment of (FM ordering) Mn^{2+} ions magnetic moments in various chains within the overlapping BMPs (Figure 8).^{38, 40, 54} Long-range FM interaction is established when the density of localized electrons is sufficiently high to allow intra-chain and inter-chain coupling between Mn^{2+} ions in various magnetic. As shown in Figure 8, moments of spin-polarized hydrogenic electrons can be located on Sb sites separating adjacent Mn^{2+} ions the crystal structure. The short distance between neighboring Sb sites facilitates the overlapping of the orbit of the neighboring BMPs even for a small density of localized hydrogenic electrons. In $\text{MnSb}_{2-x}\text{Sn}_x\text{Se}_4$ compositions, this situation is realized for $0.05 \leq x \leq 0.15$. The concentration of localized electrons in compositions with lower Sn content ($x < 0.05$) is probably too low to support long-range FM ordering. For compositions with higher Sn content ($x > 0.15$), the concentration of acceptor states occupied by electrons is sufficiently large to enable overlap between their orbitals. This results in the formation of an impurity band with delocalized electrons. Such delocalization breaks the AFM interactions between Mn^{2+} ions and hydrogenic electrons, and establishes continuous paths joining nearest-neighbor magnetic ions. As a consequence, local FM interaction

between neighboring Mn^{2+} ions observed when they are within the orbit of the same localized electron vanishes leading to AFM or ferrimagnetic interactions.

4. Conclusion

In summary, we have systematically investigated the correlation between the electronic transport properties and the predominant magnetic ordering mechanism in Sn-doped *p*-type $\text{MnSb}_{2-x}\text{Sn}_x\text{Se}_4$ phases. We found that the partial substitution of Sb^{3+} by Sn^{2+} in the structure of MnSb_2Se_4 induces the oxidation of a fraction of the remaining Sb^{3+} ions into Sb^{5+} . The Sb/Sn substitution creates a large concentration of acceptor states within the band gap, while the accompanying oxidation process generates a high density of electrons within the *p*-type $\text{MnSb}_{2-x}\text{Sn}_x\text{Se}_4$ phases. This alteration of the electronic properties of $\text{MnSb}_{2-x}\text{Sn}_x\text{Se}_4$ results in large increases in the electrical resistivity and thermopower, which is associated with a decrease in the overall hole density due to electron-hole compensation processes. Surprisingly, the dominant magnetic behavior switches from the AFM exchange interaction observed in un-substituted MnSb_2Se_4 phase to FM interaction with a Curie temperature $T_c = 56$ K in the samples with optimum Sn concentration ($0.05 \leq x \leq 0.15$) and vanishes with further increase in *x*. The observed remarkable alteration of the dominant magnetic interaction in $\text{MnSb}_{2-x}\text{Sn}_x\text{Se}_4$ phases from AFM to FM and back to AFM upon increasing Sn concentration is rationalized within the context of spin-polarization and localization of hydrogenic electrons (acceptor states populated by added electrons) at low temperatures and their interaction with 3d moments of Mn^{2+} ions to form BMPs. At the optimum density of localized hydrogenic electrons ($0.05 \leq x \leq 0.15$), neighboring BMPs overlap and interact with each other via shared spin-polarized electrons. This interaction produces alignment of the polaron spins, and FM interaction occurs when sufficiently large polarons are formed and overlap. For compositions with high Sn content ($x > 0.15$), the large concentration of acceptor states and high density of electrons generated result in the formation of an impurity band with delocalized spin-polarized electrons. This breaks the BMPs and establishes continuous paths joining nearest-neighbor magnetic ions leading to predominantly AFM interaction.

Acknowledgements

This work was supported by the National Science Foundation Career Award DMR-1237550. CU and PFPP also gratefully acknowledge financial support from the Department of Energy, Office of Basic Energy Sciences under Award # DE-SC-0008574. DPY acknowledges support from the NSF under grant # DMR-1306392. Magnetic data were recorded on a

SQUID magnetometer at the University of Michigan purchased using a MRI grant from the NSF (CHE-104008).

References

- 1 R. Cadenas, F. V. Perez, M. Quintero, E. Quintero, R. Tovar, M. Morocoima, J. Gonzalez, P. Bocaranda, J. Ruiz, J. M. Broto, H. Rakoto, Magnetic properties of the semimagnetic semiconductor $\text{Zn}_{0.15}\text{Mn}_{0.85}\text{Ga}_2\text{Se}_4$, *Physica B-Condensed Matter*, 2007, **389**, 302.
- 2 E. L. Nagaev, *Colossal Magnetoresistance and Phase separation in Magnetic Semiconductors*, Imperial college Press, 2002.
- 3 E. Quintero, M. Quintero, M. Morocoima, P. Bocaranda, Bound magnetic polarons in p-type $\text{Cu}_2\text{Cd}_{0.25}\text{Fe}_{0.75}\text{GeSe}_4$ and $\text{Cu}_2\text{FeGeTe}_4$, *Journal of Applied Physics*, 2007, **102**, 083905
- 4 M. Berciu, R. N. Bhatt, Effects of disorder on ferromagnetism in diluted magnetic semiconductors, *Physical Review Letters*, 2001, **87**, 107203.
- 5 M. Venkatesan, C. B. Fitzgerald, J. G. Lunney, J. M. D. Coey, Anisotropic ferromagnetism in substituted zinc oxide, *Physical Review Letters*, 2004, **93**, 177206.
- 6 J. M. D. Coey, M. Venkatesan, C. B. Fitzgerald, Donor impurity band exchange in dilute ferromagnetic oxides, *Nature Materials*, 2005, **4**, 173.
- 7 Y. Matsumoto, Room-temperature ferromagnetism in transparent transition metal-doped titanium dioxide *Science*, 2001, **294**, 1003.
- 8 V. I. Litvinov, V. K. Dugaev, Ferromagnetism in magnetically doped III-V semiconductors, *Physical Review Letters*, 2001, **86**, 5593.
- 9 C. Anglin, N. Takas, J. Callejas, P. F. P. Poudeu, Crystal structure and physical properties of the quaternary manganese-bearing pavonite homologue $\text{Mn}_{1.34}\text{Sn}_{6.66}\text{Bi}_8\text{Se}_{20}$, *Journal of Solid State Chemistry*, 2010, **183**, 1529.
- 10 Y. Matsushita, Y. Ueda, Structure and physical properties of 1D magnetic chalcogenide, jamesonite ($\text{FePb}_4\text{Sb}_6\text{S}_{14}$), *Inorganic Chemistry*, 2003, **42**, 7830.
- 11 P. F. P. Poudeu, N. Takas, C. Anglin, J. Eastwood, A. Rivera, $\text{Fe}_x\text{Pb}_{4-x}\text{Sb}_4\text{Se}_{10}$: A New Class of Ferromagnetic Semiconductors with Quasi 1D $[\text{Fe}_2\text{Se}_{10}]$ Ladders, *Journal of the American Chemical Society*, 2010, **132**, 5751.
- 12 A. Kaminski, S. Das Sarma, Magnetic and transport percolation in diluted magnetic semiconductors, *Physical Review B*, 2003, **68**, 235210.

- 13 A. H. Macdonald, P. Schiffer, N. Samarth, Ferromagnetic semiconductors: moving beyond (Ga, Mn)As, *Nature Materials*, 2005, **4**, 195.
- 14 T. Dietl, H. Ohno, F. Matsukura, J. Cibert, D. Ferrand, Zener model description of ferromagnetism in zinc-blende magnetic semiconductors, *Science*, 2000, **287**, 1019.
- 15 Z. H. Zhou, Y. J. Chien, C. Uher, Thin film dilute ferromagnetic semiconductors $\text{Sb}_{2-x}\text{Cr}_x\text{Te}_3$ with a Curie temperature up to 190 K, *Physical Review B*, 2006, **74**, 224418.
- 16 Z. H. Zhou, Y. J. Chien, C. Uher, Thin-film ferromagnetic semiconductors based on $\text{Sb}_{2-x}\text{V}_x\text{Te}_3$ with TC of 177 K, *Applied Physics Letters*, 2005, **87**, 112503.
- 17 I. N. Goncharenko, I. Mirebeau, Ferromagnetic interactions in EuS and EuSe studied by neutron diffraction at pressures up to 20.5 GPa, *Physical Review Letters*, 1998, **80**, 1082.
- 18 J. S. Moodera, R. Meservey, X. Hao, Variation of the Electron-Spin Polarization in Euse Tunnel-Junctions from Zero to near 100-Percent in a Magnetic-Field, *Physical Review Letters*, 1993, **70**, 853.
- 19 N. Sanford, R. W. Davies, A. Lempicki, W. J. Miniscalco, S. J. Nettel, Influence of Polarized Optical-Pumping on the Ferromagnetism of CdCr_2Se_4 , *Physical Review Letters*, 1983, **50**, 1803.
- 20 J. S. Dyck, P. Hajek, P. Losit'ak, C. Uher, Diluted magnetic semiconductors based on $\text{Sb}_{2-x}\text{V}_x\text{Te}_3$ ($0.01 \leq x \leq 0.03$), *Physical Review B*, 2002, **65**, 115212.
- 21 T. Dietl, A ten-year perspective on dilute magnetic semiconductors and oxides, *Nature Materials*, 2010, **9**, 965.
- 22 S. Sanvito, N. A. Hill, Influence of the local As antisite distribution on ferromagnetism in (Ga, Mn)As, *Applied Physics Letters*, 2001, **78**, 3493.
- 23 F. Pan, C. Song, X. J. Liu, Y. C. Yang, F. Zeng, Ferromagnetism and possible application in spintronics of transition-metal-doped ZnO films, *Materials Science & Engineering R-Reports*, 2008, **62**, 1.
- 24 M. Dobrowolska, K. Tivakornsasithorn, X. Liu, J. K. Furdyna, M. Berciu, K. M. Yu, W. Walukiewicz, Controlling the Curie temperature in (Ga,Mn) As through location of the Fermi level within the impurity band, *Nature Materials*, 2012, **11**, 444.
- 25 Y. Nishitani, D. Chiba, M. Endo, M. Sawicki, F. Matsukura, T. Dietl, H. Ohno, Curie temperature versus hole concentration in field-effect structures of $\text{Ga}_{1-x}\text{Mn}_x\text{As}$, *Physical Review B*, 2010, **81**, 045208.
- 26 T. Jungwirth, J. Konig, J. Sinova, J. Kucera, A. H. MacDonald, Curie temperature trends in (III,Mn)V ferromagnetic semiconductors, *Physical Review B*, 2002, **66**, 012402.

- 27 D. Neumaier, M. Turek, U. Wurstbauer, A. Vogl, M. Utz, W. Wegscheider, D. Weiss, All-Electrical Measurement of the Density of States in (Ga,Mn)As, *Physical Review Letters*, 2009, **103**, 087203.
- 28 T. Jungwirth, J. Sinova, A. H. MacDonald, B. L. Gallagher, V. Novak, K. W. Edmonds, A. W. Rushforth, R. P. Campion, C. T. Foxon, L. Eaves, E. Olejnik, J. Masek, S. R. E. Yang, J. Wunderlich, C. Gould, L. W. Molenkamp, T. Dietl, H. Ohno, Character of states near the Fermi level in (Ga,Mn)As: Impurity to valence band crossover, *Physical Review B*, 2007, **76**, 125206.
- 29 A. Richardella, P. Roushan, S. Mack, B. Zhou, D. A. Huse, D. D. Awschalom, A. Yazdani, Visualizing Critical Correlations Near the Metal-Insulator Transition in $\text{Ga}_{1-x}\text{Mn}_x\text{As}$, *Science*, 2010, **327**, 665.
- 30 M. Sawicki, D. Chiba, A. Korbecka, Y. Nishitani, J. A. Majewski, F. Matsukura, T. Dietl, H. Ohno, Experimental probing of the interplay between ferromagnetism and localization in (Ga, Mn)As, *Nature Physics*, 2010, **6**, 22.
- 31 L. P. Rokhinson, Y. Lyanda-Geller, Z. Ge, S. Shen, X. Liu, M. Dobrowolska, J. K. Furdyna, Weak localization in $\text{Ga}_{1-x}\text{Mn}_x\text{As}$: Evidence of impurity band transport, *Physical Review B*, 2007, **76**, 161201.
- 32 M. A. Mayer, P. R. Stone, N. Miller, H. M. Smith, O. D. Dubon, E. E. Haller, K. M. Yu, W. Walukiewicz, X. Liu, J. K. Furdyna, Electronic structure of $\text{Ga}_{1-x}\text{Mn}_x\text{As}$ analyzed according to hole-concentration-dependent measurements, *Physical Review B*, 2010, **81**, 045205.
- 33 K. Alberi, K. M. Yu, P. R. Stone, O. D. Dubon, W. Walukiewicz, T. Wojtowicz, X. Liu, J. K. Furdyna, Formation of Mn-derived impurity band in III-Mn-V alloys by valence band anticrossing, *Physical Review B*, 2008, **78**, 075201.
- 34 S. C. Erwin, A. G. Petukhov, Self-compensation in manganese-doped ferromagnetic semiconductors, *Physical Review Letters*, 2002, **89**, 227201.
- 35 P. Mahadevan, A. Zunger, Trends in ferromagnetism, hole localization, and acceptor level depth for Mn substitution in GaN, GaP, GaAs, and GaSb, *Applied Physics Letters*, 2004, **85**, 2860.
- 36 R. R. Heikes, C. W. Chen, Evidence for Impurity Bands in La-Doped Eus, *Physics*, 1964, **1**, 159.
- 37 H. F. Li, Y. G. Xiao, B. Schmitz, J. Persson, W. Schmidt, P. Meuffels, G. Roth, T. Bruckel, Possible magnetic-polaron-switched positive and negative magnetoresistance in the GdSi single crystals, *Scientific Reports*, 2012, **2**, 1.

- 38 A. C. Durst, R. N. Bhatt, P. A. Wolff, Bound magnetic polaron interactions in insulating doped diluted magnetic semiconductors, *Physical Review B*, 2002, **65**, 235205.
- 39 F. Nasirpour, A. Nogoret, in *Fabrication, Materials, Characterization and Application* (Ed.: W. Scientific), Word Scientific Publishing Co.Pte.Ltd, Singapore, 2009.
- 40 P. A. Wolff, R. N. Bhatt, A. C. Durst, Polaron-polaron interactions in diluted magnetic semiconductors, *Journal of Applied Physics*, 1996, **79**, 5196.
- 41 H. Djieutedjeu, J. P. A. Makongo, A. Rotaru, A. Palasyuk, N. J. Takas, X. Y. Zhou, K. G. S. Ranmohotti, L. Spinu, C. Uher, P. F. P. Poudeu, Crystal Structure, Charge Transport, and Magnetic Properties of MnSb_2Se_4 , *European Journal of Inorganic Chemistry*, 2011, 3969.
- 42 H. Djieutedjeu, P. F. P. Poudeu, N. J. Takas, J. P. A. Makongo, A. Rotaru, K. G. S. Ranmohotti, C. J. Anglin, L. Spinu, J. B. Wiley, Structural-Distortion-Driven Cooperative Magnetic and Semiconductor-to-Insulator Transitions in Ferromagnetic FeSb_2Se_4 , *Angewandte Chemie-International Edition*, 2010, **49**, 9977.
- 43 A. Mrozek, M. G. Kanatzidis, "Design" in solid-state chemistry based on phase homologies. The concept of structural evolution and the new megaserie $A_m[M_{1+i}\text{Se}_{2+i}]_{2m}[M_{21+n}\text{Se}_{2+31+n}]$, *Accounts of Chemical Research*, 2003, **36**, 111.
- 44 P. F. P. Poudeu, H. Djieutedjeu, P. Sahoo, Crystal Structure of $\text{FePb}_4\text{Sb}_6\text{Se}_{14}$ and its Structural Relationship with $\text{FePb}_3\text{Sb}_4\text{Se}_{10}$, *Zeitschrift Fur Anorganische Und Allgemeine Chemie*, 2012, **638**, 2549.
- 45 K. G. S. Ranmohotti, H. Djieutedjeu, P. F. P. Poudeu, Chemical Manipulation of Magnetic Ordering in $\text{Mn}_{1-x}\text{Sn}_x\text{Bi}_2\text{Se}_4$ Solid-Solutions, *Journal of the American Chemical Society*, 2012, **134**, 14033.
- 46 J. Rodriguez-Carvajal, Recent advances in magnetic Structure determination by neutron powder diffraction, *Physica B-Condensed Matter*, 1993, **192**, 55.
- 47 J. Rodriguez-Carvajal, Recent Developments of the Program FULLPROF, in Commission on Powder Diffraction (IUCr), *Newsletter*, 2001, **26**, 12.
- 48 R. D. Shannon, Revised Effective Ionic-Radii and Systematic Studies of Interatomic Distances in Halides and Chalcogenides, *Acta Crystallographica Section A*, 1976, **32**, 751.
- 49 R. D. Shannon, C. T. Prewitt, Effective Ionic Radii in Oxides and Fluorides, *Acta Crystallographica Section B-Structural Crystallography and Crystal Chemistry*, 1969, **B 25**, 925.

- 50 W. X. Zhang, Z. H. Yang, J. W. Liu, L. Zhang, Z. H. Hui, W. C. Yu, Y. T. Qian, L. Chen, X. M. Liu, Room temperature growth of nanocrystalline tin (II) selenide from aqueous solution, *Journal of Crystal Growth*, 2000, **217**, 157.
- 51 H. Franzen, C. Sterner, X-Ray Photoelectron-Spectra of MnS, MnSe, and MnTe, *Journal of Solid State Chemistry*, 1978, **25**, 227.
- 52 O. Savadogo, K. C. Mandal, Studies on New Chemically Deposited Photoconducting Antimony Trisulfide Thin-Films, *Solar Energy Materials and Solar Cells*, 1992, **26**, 117.
- 53 D. K. Kim, J. H. Lee, Y. W. Heo, H. Y. Lee, J. J. Kim, Co-doping effect of Zn and Sb in SnO₂: Valence stabilization of Sb and expanded solubility limit, *Ceramics International*, 2011, **37**, 2723.
- 54 A. Kaminski, S. Das Sarma, Polaron percolation in diluted magnetic semiconductors, *Physical Review Letters*, 2002, **88**, 247202.

Figures

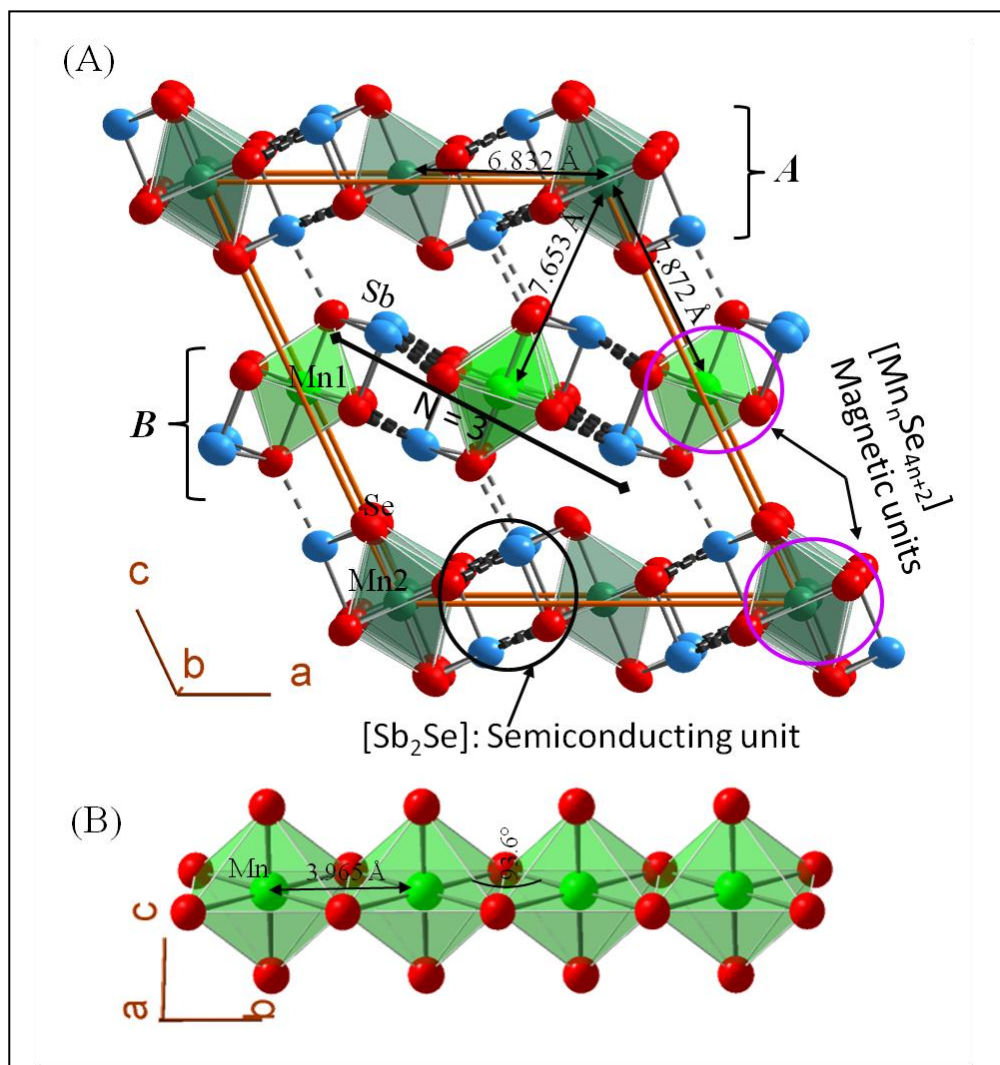


Figure 1. (A) Crystal structure of $\text{MnSb}_{2-x}\text{Sn}_x\text{Se}_4$ projected along the b -axis highlighting the structural distribution of the semiconducting and magnetic units. (B) Structure of the magnetic unit highlighting the $[\text{Mn}_n\text{Se}_{4n+2}]$ 1D chain edge-sharing Mn centered octahedral. Adapted from ref# 40

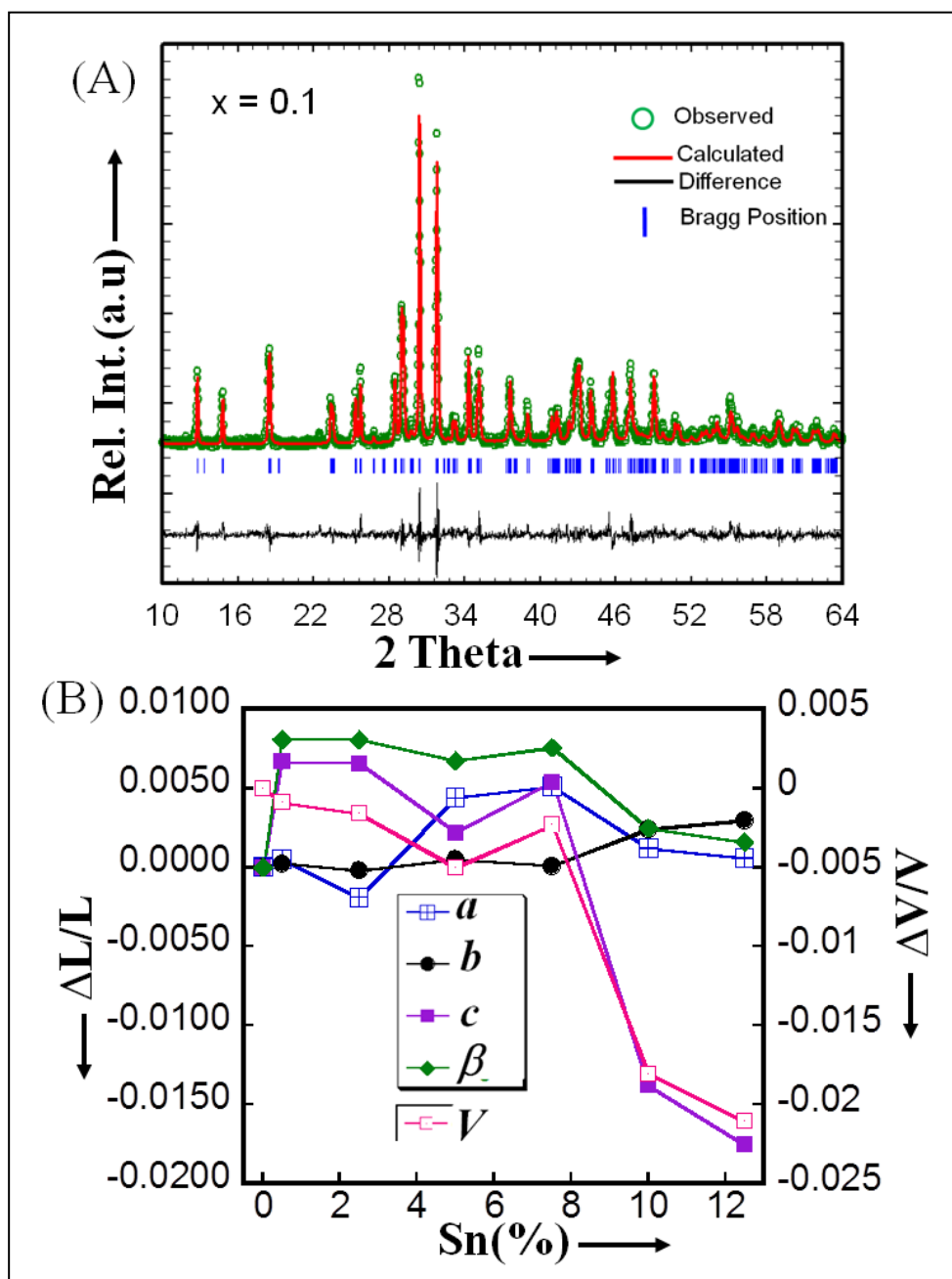


Figure 2. (A) X-ray powder diffraction data of $\text{MnSb}_{2-x}\text{Sn}_x\text{Se}_4$ ($x = 0.1$) generated by Rietveld refinement, showing excellent match between observed and calculated patterns. Similar plots were obtained for the remaining compositions. (B) Relative change in the unit cell parameters and volume of $\text{MnSb}_{2-x}\text{Sn}_x\text{Se}_4$ as a function of Sn concentration.

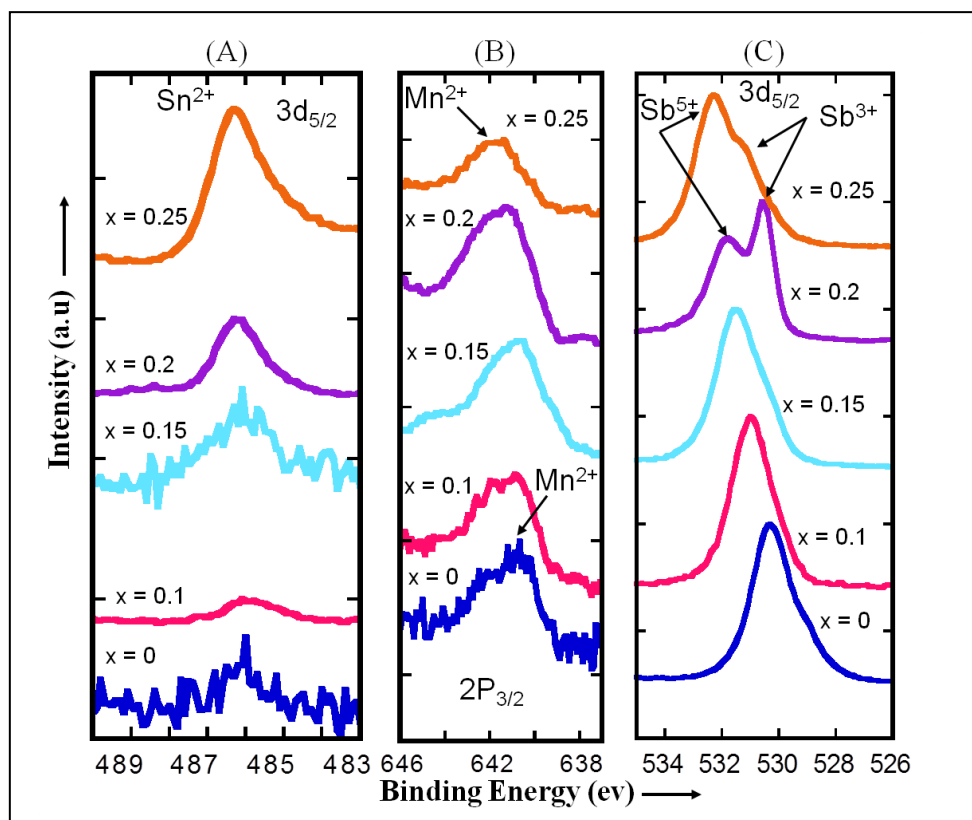


Figure 3. XPS spectra of selected $\text{MnSb}_{2-x}\text{Sn}_x\text{Se}_4$ samples. (A) Sn $3d_{5/2}$ peak; (B) Mn $2P_{3/2}$ peak; (C) Sb $3d_{5/2}$ peaks for Sb^{3+} and Sb^{5+} .

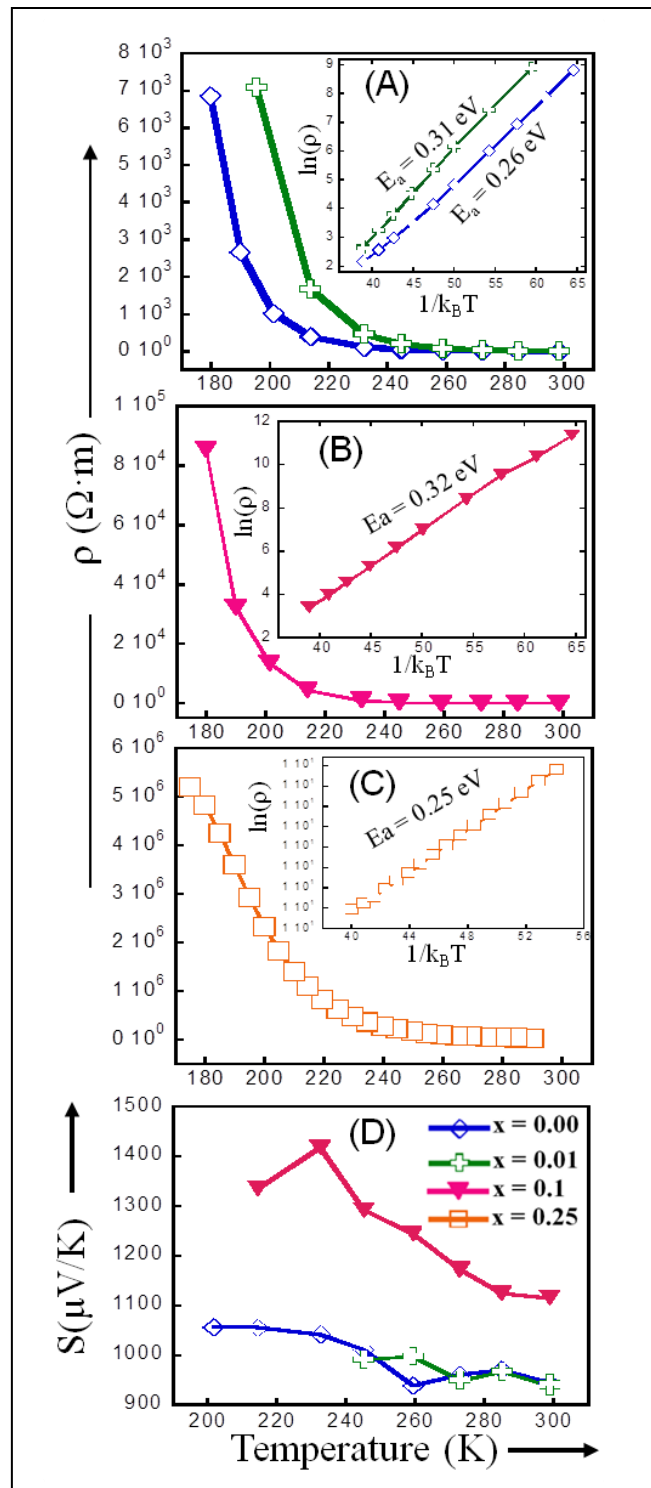


Figure 4. Temperature dependence of the electronic transport properties of $\text{MnSb}_{2-x}\text{Sn}_x\text{Se}_4$. Electrical resistivity of samples with (A) $x = 0$ and $x = 0.01$; (B) $x = 0.1$; and (C) $x = 0.25$. (D) Thermopower of selected $\text{MnSb}_{2-x}\text{Sn}_x\text{Se}_4$ ($0 \leq x \leq 0.25$) compositions.

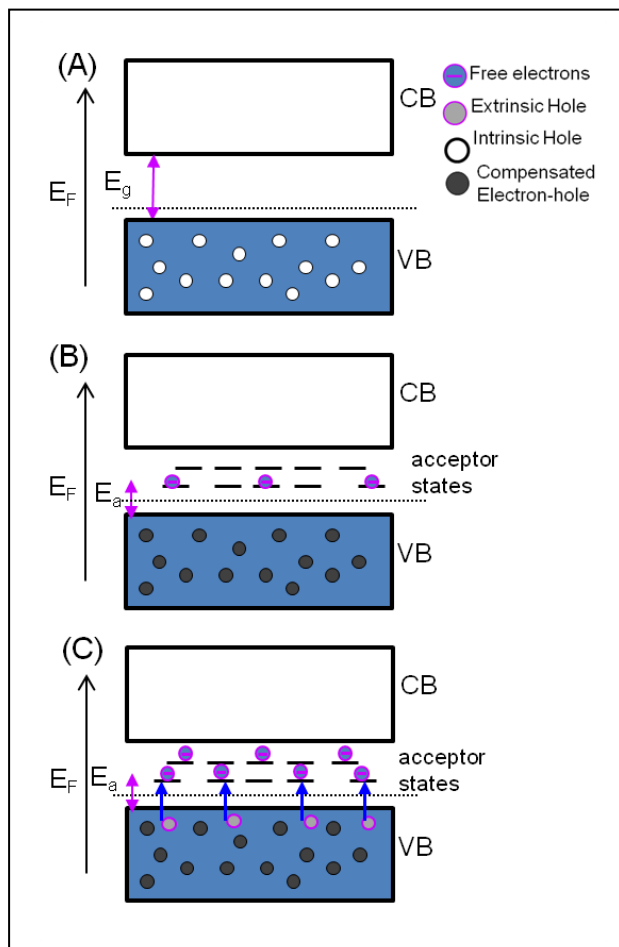


Figure 5. Proposed band structure model for the understanding of electronic transport and magnetism in MnSb_{2-x}Sn_xSe₄. (A) Un-substituted *p*-type MnSb₂Se₄ at T = 0 K; (B) Sn-substituted *p*-type MnSb_{2-x}Sn_xSe₄ (x > 0) at T = 0 K showing compensated electron-hole pairs and hydrogenic electrons within the band gap ; (C) Sn-substituted *p*-type MnSb_{2-x}Sn_xSe₄ (x > 0) at T > 0 K showing thermal excitation of electrons from the top of the valence band to the acceptor states within the band gap.

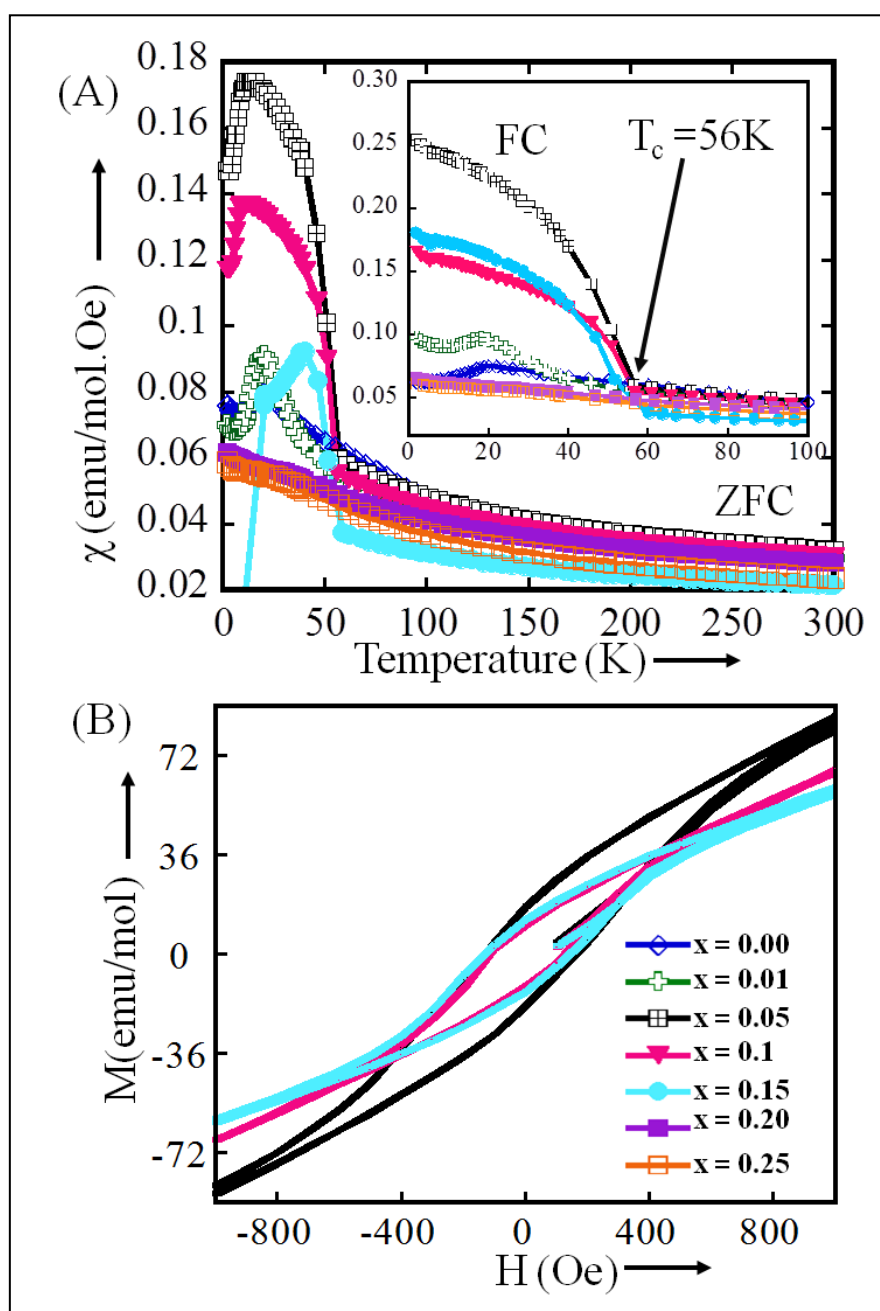


Figure 6. DC magnetic properties of $\text{MnSb}_{2-x}\text{Sn}_x\text{Se}_4$ ($0 \leq x \leq 0.25$). (A) Temperature dependence of the zero-field-cooled (ZFC) molar magnetic susceptibility measured under applied field of 100 Oe. The inset is the corresponding field-cooled (FC) magnetic susceptibility within the temperature range 2 K-100 K. (B) Field dependent magnetization at 4 K of selected $\text{MnSb}_{2-x}\text{Sn}_x\text{Se}_4$ ($x = 0.05; 0.1; 0.15$) compositions showing broad hysteresis loops with a coercivity force of 150 Oe.

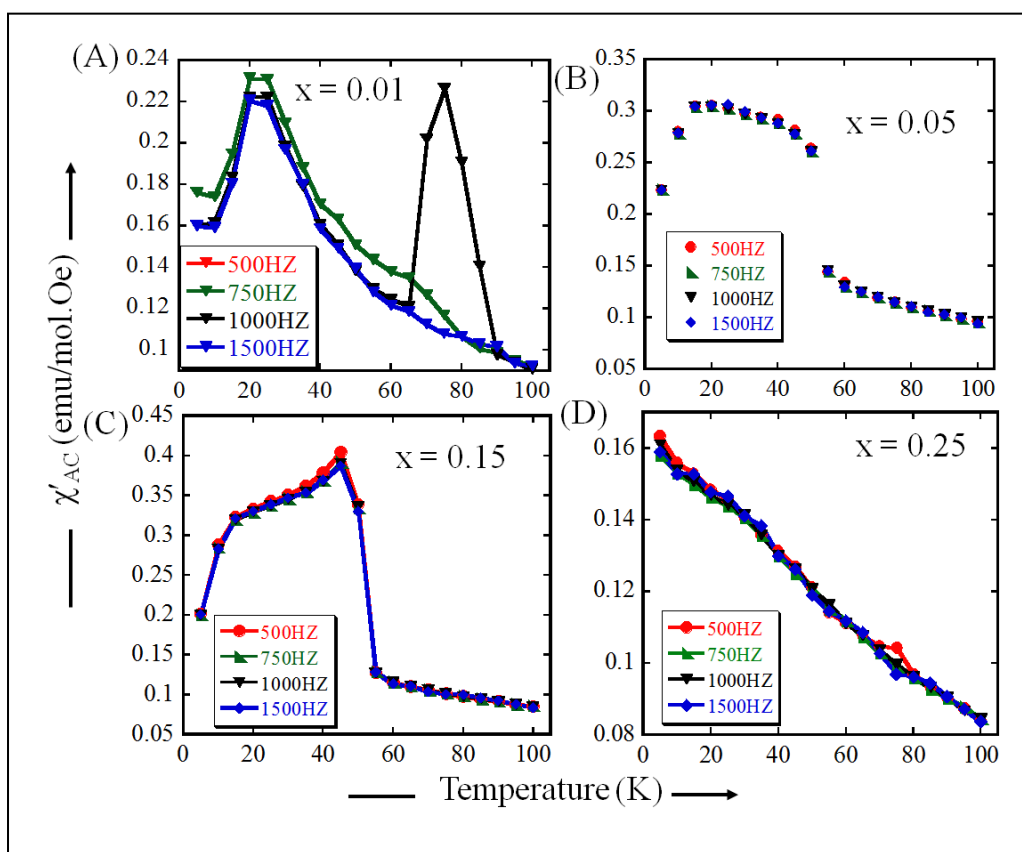


Figure 7. Temperature dependence of the in-phase component of the AC magnetic susceptibility for selected $\text{MnSb}_{2-x}\text{Sn}_x\text{Se}_4$ compositions measured at various frequencies (from 500 Hz to 1500 Hz) under an applied field of 0.1 Oe. (A): $x = 0.01$; (B): $x = 0.05$; (C): $x = 0.15$; (D): $x = 0.25$.

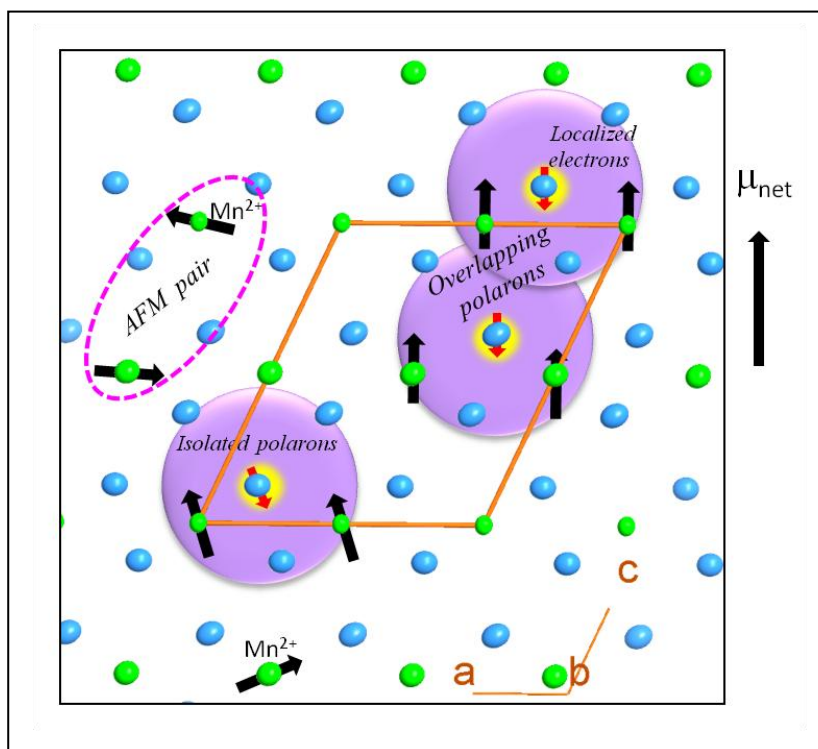


Figure 8. Proposed formation of bound magnetic polarons (BMPs) in $\text{MnSb}_{2-x}\text{Sn}_x\text{Se}_4$ structures. Moments of spin-polarized hydrogenic electrons are located on Sb sites separating adjacent Mn^{2+} ions and are coupled antiferromagnetically with Mn^{2+} ions in their orbit. The short distance between neighboring Sb sites enables overlapping of the orbit of the neighboring BMPs, even for a small density of localized hydrogenic electrons, leading to long range ferromagnetic ordering. Selenium atoms are not shown.

Tables

Table 1. Rietveld refinement and unit cell parameters of various $\text{MnSb}_{2-x}\text{Sn}_x\text{Se}_4$ compositions

Sn content (x)	0.00	0.01	0.05	0.10	0.15	0.20	0.25
Space group	Monoclinic, $C 2/m(\#12)$						
Unit cell parameters							
$a(\text{\AA})$	13.250(1)	13.257(1)	13.225(1)	13.308(2)	13.318(2)	13.266(2)	13.258(2)
$b(\text{\AA})$	3.963(2)	3.964(2)	3.963(1)	3.966(2)	3.964(1)	3.973(1)	3.976(2)
$c(\text{\AA})$	15.372(1)	15.475(2)	15.473(1)	15.406(1)	15.455(2)	15.160(1)	15.103(2)
$\beta(^{\circ})$	115.16(2)	116.09(1)	116.09(2)	115.93(2)	116.03(1)	115.44(2)	115.34(1)
Volume (\AA^3)	734.91(2)	734.26(2)	733.75(2)	731.24(2)	733.21(1)	721.64(2)	719.44(2)
R_f -factor	2.70%	6.53%	5.66%	5.71%	5.58%	7.62%	1.74%
Bragg R_f -factor	2.78%	9.58%	7.78%	7.94%	7.64%	10.3%	1.26%
χ^2	1.72	1.62	1.60	1.73	1.50	1.61	2.48

Table 2. Atomic positions of selected $\text{MnSb}_{2-x}\text{Sn}_x\text{Se}_4$ compositions

Sn content (x)	0.00			0.10			0.20		
Atom	x	y	z	x	y	z	x	y	z
Sb(1)	0.2738(2)	0	0.6334(2)	0.2728(7)	0	0.6324(4)	0.2762(7)	0	0.6361(2)
Mn(1)	0.2738(2)	0	0.6334(2)	0.2728(7)	0	0.6324(4)	0.2762(7)	0	0.6361(2)
Sb(2)	0.3554(2)	0	0.1260(2)	0.3590(1)	0	0.1281(5)	0.3524(9)	0	0.1255(7)
Mn(2)	0.3554(2)	0	0.1260(2)	0.3590(1)	0	0.1281(5)	0.3524(9)	0	0.1255(7)
Mn(3)	0	1/2	1/2	0	1/2	0.5000(0)	0	1/2	1/2
Sb(4)	0	0	0	0	0	0	0	0	0
Mn(4)	0	0	0	0	0	0	0	0	0
Se(1)	0.0123(2)	0	0.1799(2)	0.0133(7)	0	0.1801(7)	0.0136(8)	0	0.1801(9)
Se(2)	0.1143(2)	0	0.4575(2)	0.1114(0)	0	0.4547(5)	0.1122(0)	0	0.4526(9)
Se(3)	0.3446(2)	0	0.3277(2)	0.3345(3)	0	0.3233(6)	0.3387(3)	0	0.3181(4)
Se(4)	0.6549(2)	0	0.0533(2)	0.6665(5)	0	0.0588(1)	0.6590(7)	0	0.0575(4)

Table 3. Curie constant, Weiss constant and the effective magnetic moments extracted from the linear fits of the inverse susceptibility data of $\text{MnSb}_{2-x}\text{Sn}_x\text{Se}_4$.

Sn content (x)	Curie Constant (emu K mol ⁻¹)	Weiss Constant (K)	Effective Magnetic Moment (μ_B)
x= 0.0	5.48	-74	5.82
x=0.01	5.66	-41	6.73
x=0.05	5.03	-0.9	6.34
x=0.1	4.96	-8.8	6.30
x=0.15	4.01	1.2	5.66
x=0.20	5.67	-102	6.59
x=0.25	7.89	-99	7.94

Table of Contents Synopsis

Sb^{3+} to Sn^{2+} substitution generates acceptors and donors in MnSb_2Se_4 matrix leading to localized hydrogenic electrons, which couple with Mn^{2+} ions to induce ferromagnetism in samples with optimum Sn content.

